Ceramics International 44 (2018) 22638–22644

Contents lists available at ScienceDirect

Ceramics International

journal homepage: www.elsevier.com/locate/ceramint

Synthesis of Bi_2O_3/TiO_2 nanostructured films for photocatalytic applications

F.C. Correia, M. Calheiros, J. Marques, J.M. Ribeiro, C.J. Tavares*

Centre of Physics, University of Minho, Guimarães, Portugal

ARTICLE INFO

Keywords:
Bi_2O_3
TiO_2
Photocatalysis
Reactive sputtering
Vapour-liquid-solid mechanism
Dendritic

ABSTRACT

Dendritic growth of bismuth oxide nanostructured films was accomplished by reactive magnetron sputtering. The deposition of the Bi_2O_3 template layers was adapted to abide a vapour-liquid-solid mechanism in order to develop a 3D growth morphology with high surface area templates for photocatalytic applications. TiO_2 photocatalytic thin films were deposited at a later stage onto Bi_2O_3 layers. The obtained heterostructured films were characterized by scanning electron microscopy, X-ray diffraction and atomic force microscopy. Additionally, the photocatalytic efficiency was assessed by conducting an assay using methylene blue dye as testing pollutant under a UV-A illumination. The photocatalytic tests revealed that the Bi_2O_3 layers functionalized with TiO_2 thin films are more efficient at degrading the pollutant, by a factor of 6, when compared with the individual layered films.

1. Introduction

The increasing scarcity of potable water has served as motivation for the development of decontamination processes [1,2]. The constant discharge of volatile organic compounds such contaminants and pollutants contaminate breathable air and reduces the number of freshwater sources suitable for consumption. These toxins are a serious problem both in the air and in drinking water distribution lines, since they are not removed by conventional treatments; only some technologies can eliminate them [1]. Photocatalytic degradation is one of the most viable processes when compared with the conventional ones [3]. This process uses the UV radiation effect to produce hydroxyl radicals, with the assistance of a photocatalyst [4]. The most commonly used catalyst is titanium dioxide, characterized by its low toxicity and high chemical stability, however. The major drawback is its high bandgap energy of 3.2 eV for the anatase dominant phase, which limits its effectiveness by absorbing radiation in the UV range alone [5]. Bismuth oxide (Bi_2O_3) has several polymorphic forms: α, β, δ, γ and ε, being α an β phase those with greater photocatalytic efficiency, with a direct band-gap energy in the range of 2.5–2.9 eV [6–9]. Some authors have reported on the photocatalytic efficiency of Bi_2O_3 [8,10–12]. A high specific surface area is developed in this material when synthetized in the form of nanocones [7], promoting the photocatalytic efficiency by creating more adsorption sites for pollutants. This is done at the semiconductor level by completing the intrinsic polarity induced by the electron pairs of Bi $6s^2$ that favours the separation of the photogenerated electron-hole pairs [13].

In this work, bismuth oxide films with fibrous morphology and high surface area were produced as templates for the deposition of thin titanium dioxide (TiO_2) overlayer thin films with photocatalytic properties. These heterostructured layers provide vital characteristics for decontamination and purification processes. By coupling both metal oxides, TiO_2 and Bi_2O_3, it is expected a heterojunction with a wider absorption spectra of solar light. Fig. 1 shows the resulting photocatalytic mechanism of a coupling between Bi_2O_3 and TiO_2, wherein both initially absorb UV–Vis light to form the electron-hole pairs, thereby reducing the recombination of electrons-holes. Since the conduction and valence bands of TiO_2 are less anodic than those of Bi_2O_3, the excited electrons in TiO_2 can be transferred to Bi_2O_3 [14]. To do so, in this manuscript is described the procedure for the optimization of magnetron reactive sputtering deposition process parameters in order to obtain Bi_2O_3 films through vapour-liquid-solid mechanism (VLS) [15], which resulted in the growth of nanocones with a rough 3D morphology with a high surface area. Subsequently, a very thin TiO_2 film with known photocatalytic properties [16,17] was sputtered onto the Bi_2O_3 layer. The resulting Bi_2O_3/TiO_2 nanostructured thin films morphology was characterized by scanning electron microscopy (SEM). Surface roughness and projected surface area of these films was determined by atomic force microscopy. The crystal structures and the size of the crystallites were determined by X-ray diffraction. As for the evaluation of the photocatalytic performance, this was performed in a UV-A reactor in the presence of a test pollutant (methylene blue) and the respective degradation kinetics were recorded.

* Corresponding author.
E-mail address: ctavares@fisica.uminho.pt (C.J. Tavares).

https://doi.org/10.1016/j.ceramint.2018.09.040
Received 16 July 2018; Received in revised form 4 September 2018; Accepted 5 September 2018
Available online 06 September 2018

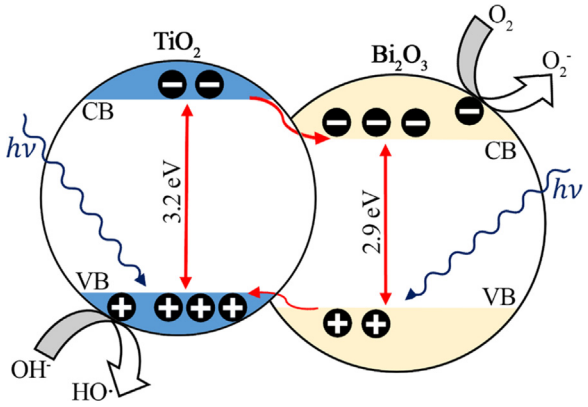

Fig. 1. Suggested photocatalytic mechanism for a Bi_2O_3/TiO_2 heterostructured material.

Table 1
Process parameters for the deposition of Bi/Bi_2O_3 films.

Base pressure in chamber	10^{-4} Pa
Deposition temperature	RT, 175 °C
Bi seed layer deposition rate	180 nm/min.
Bi_2O_3 layer deposition rate	340 nm/min.
Cathode DC current density	5.0 mA/cm^2
Substrate bias voltage	- 40 V
Target-substrate distance	6 cm
Argon partial pressure	0.50 Pa
Oxygen partial pressure	0.05–0.11 Pa

Table 2
Process parameters for the deposition of TiO_2 thin films.

Base pressure in chamber	10^{-4} Pa
Deposition temperature	175 °C
TiO_2 layer deposition rate	6 nm/min.
Cathode DC current density	12.5 mA/cm^2
Substrate bias voltage	- 40 V
Target-substrate distance	6 cm
Argon partial pressure	0.50 Pa
Oxygen partial pressure	0.03 Pa

2. Materials and methods

2.1. Deposition techniques

The VLS growth mechanism occurs due to adsorption of gaseous reactants in a liquid metal droplet, which acts as catalyst of the involved process. The metallic drop can adsorb the vapour, however the adsorption is limited. If there is sufficient vapour the drop can become supersaturated, generating nucleation [18]. Once a core is first formed, the growth is driven by this core and monocrystalline structures are formed on a diameter of the metallic droplet [18]. In this process, a metal catalyst is rationally chosen and serves as a site for the adsorption of the formed compounds, but should not form a solid solution with the nanowire (or nanocone) [19]. In the present case, the bismuth liquid metal droplet serves as a preferential site, or seed, for the adsorption of the reagent in gaseous phase (oxygen). As seen in Fig. 2, the growth of Bi_2O_3 nanocones develops after the Bi liquid reagent becomes supersaturated and continues while this metal catalyst remains in the liquid

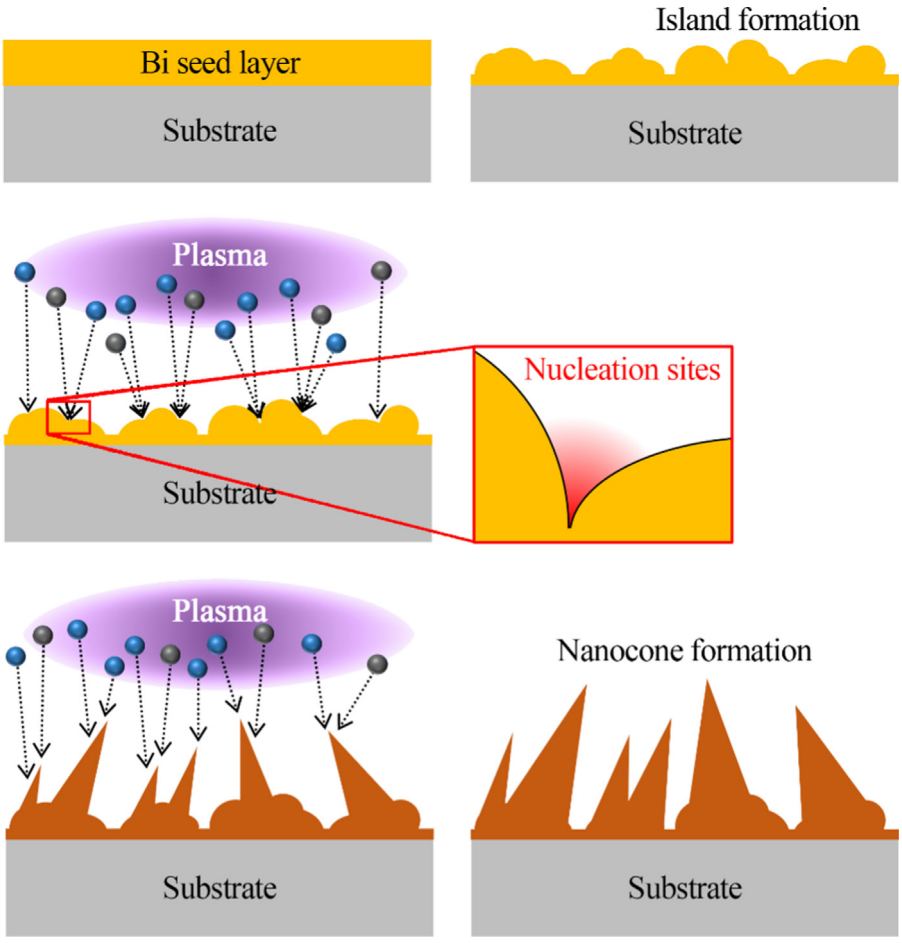

Fig. 2. VLS-induced growth model of dendritic Bi/Bi_2O_3 films by magnetron sputtering (Adapted [21]).

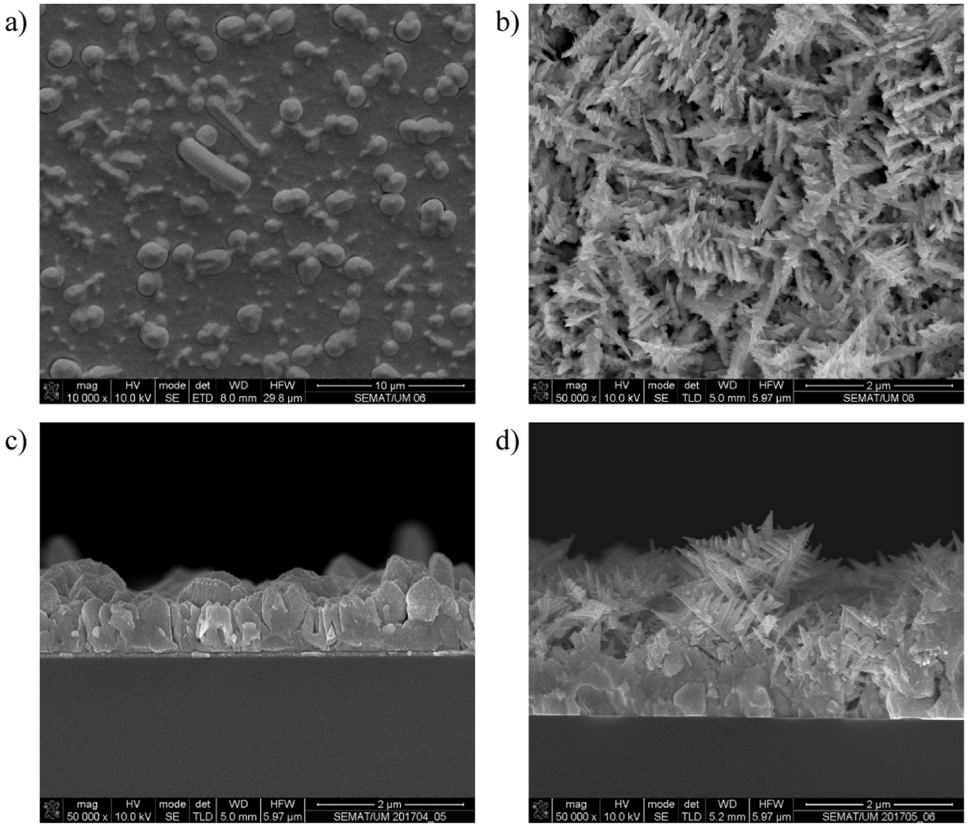

Fig. 3. SEM micrographs taken from the surface of Bi/Bi_2O_3 layers deposited with an oxygen (reactant) partial pressure of 0.11 Pa at: a) room temperature (RT) and b) 175 °C. In c) and d): respective cross-sections.

state and there is availability of oxygen. During growth, the Bi catalyst droplet drives the growth direction of the nanocones and defines its diameter [18,20,21].

The depositions were performed on silicon and glass substrates, with and without (RT) intentional substrate heating, by reactive magnetron sputtering using a custom made high-vacuum chamber with a base pressure of $\sim 10^{-4}$ Pa. Two metal targets were used as cathodes, Bi and Ti of high purity (99.95%) and (99.8%), respectively, having dimensions of 100 mm (diameter) × 6 mm (thickness). The substrates were all cleaned with isopropyl in an ultrasonic bath for ~15 min before loading into the deposition chamber. Prior to deposition, a plasma etching at a pressure of 2 Pa was performed during 3 min in order to eliminate adventitious impurities accumulated on the surface of the substrates and targets. The initial depositions were carried out with the purpose of evaluating the effect of deposition pressure, substrate temperature, deposition time, reactive and working gas partial pressures on the formation of heterostructured films. The process parameters for the Bi_2O_3 layer are listed in Table 1. The deposition process parameters for the initial Bi seed layer were kept constant before introducing the reactant oxygen gas in the chamber for the subsequent Bi_2O_3 layer formation by VLS. The photocatalytic TiO_2 layer was deposited in a different run, for varying thickness between 6 and 30 nm, with the same process parameters, as identified in Table 2. No subsequent thermal annealing was performed on the as-deposited films.

2.2. Materials characterization

The crystalline structure of the film layers was characterized using X-ray diffraction analysis (XRD, Bruker D8 Discover diffractometer) by means of CuKα radiation, while the morphological properties were studied using a scanning electron microscope (SEM, NanoSEM-FEI Nova 200). The optical transmittance and reflectance was measured with a Shimadzu UV-2501PC spectrophotometer. To assess the nanostructured layers surface roughness an atomic force microscope (AFM, Digital Instruments Nanoscope III) was used. In order to evaluate the photocatalytic activity of the different heterostructured film samples, the photocatalytic oxidation of methylene blue (MB) in the presence of the under UV-A irradiation was studied. The experiments were carried out by immersing the sample in aqueous methylene blue solution (10^{-5} M) in a quartz cell ($40 \times 40 \times 10\ mm^3$), under UV-A radiation centred at 365 nm with a high power LED source (Thorlabs, 700 mA), with an average irradiance of $2\ mW/cm^2$. The rate of photo-degradation of MB is related to the variation in intensity of the absorption peak of this chromophore at 665 nm, which was analysed using a spectrophotometer (ScanSpec UV–Vis, ScanSci) in the range of 300–900 nm, with an auxiliary Hamamatsu Model L10761 light source.

3. Results and discussion

Fig. 3 shows the surface and cross-sectional morphologies of Bi_2O_3 layers grown by VLS from a starting Bi seed layer. The initial Bi seed layer was magnetron sputtered in an argon atmosphere with a deposition rate of 180 nm/min during 2 min. After this period, oxygen was inlet with varying partial pressure in the range of 0.05–0.11 Pa, resulting in a maximum deposition rate of 340 nm/min for the Bi_2O_3 layer, while maintaining all other deposition process parameters constant (Table 1). It can be observed from Fig. 3b) that when the substrate holder is heated the nanocone formation is more dendritic, resembling pine tree-like nanostructures, whereas for the deposition at RT (Fig. 3a) only random Bi/Bi_2O_3 islands are discerned. In Fig. 3c) and d) it is possible to observe SEM micrographs of the cross-section of the films displayed in Fig. 3a) and b), respectively, further evidencing the development of 3D islands at RT in contrast with the dendritic structures that grow at 175 °C.

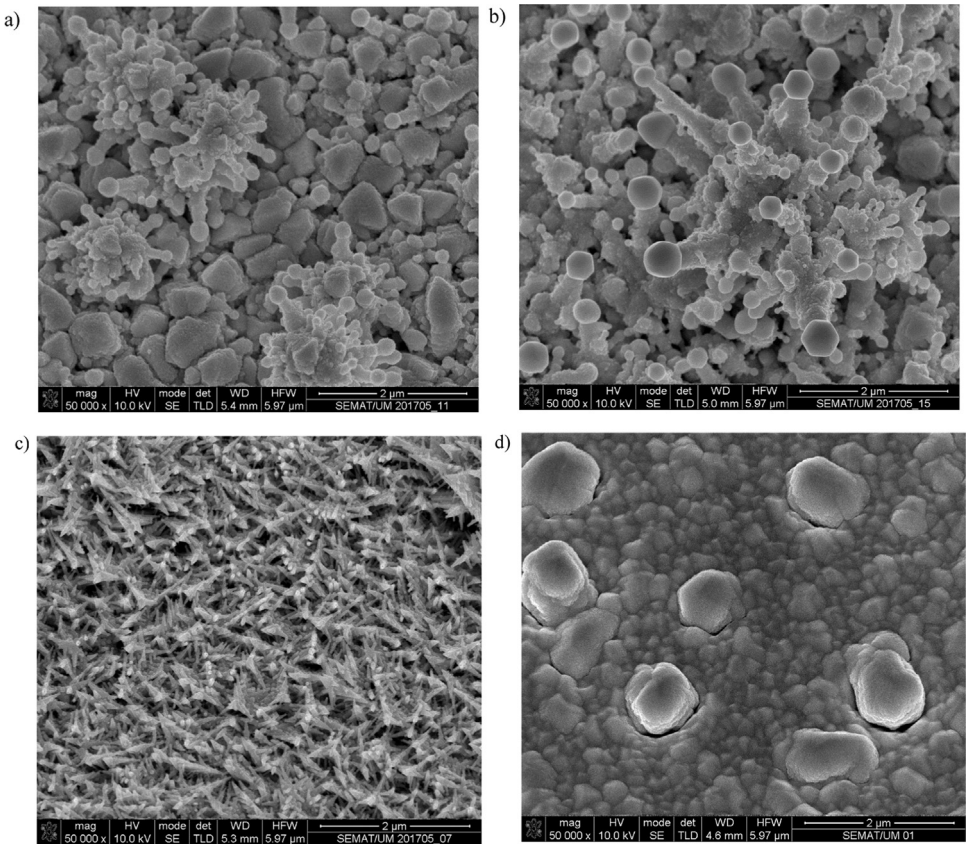

Fig. 4. SEM micrographs taken from the surface of Bi/Bi_2O_3 layers deposited at 175 °C with varying oxygen partial pressure: a) 0.05 Pa; b) 0.07 Pa; c) 0.11 Pa. From c) to d) only the total pressure is varied from 0.51 Pa to 0.90 Pa.

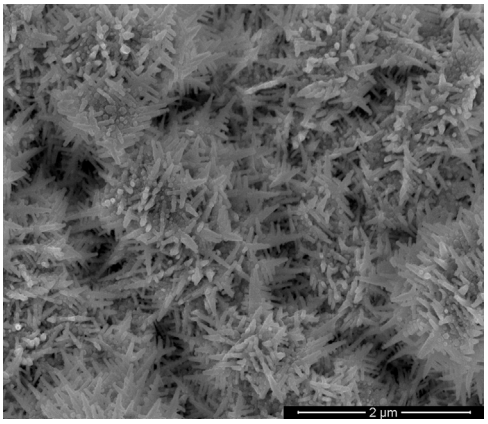

Fig. 5. SEM micrograph taken from the surface of a $Bi/Bi_2O_3/TiO_2$ film.

In Fig. 4a)-c) it is possible to observe SEM micrographs of the surface morphologies of Bi/Bi_2O_3 layers deposited at 175 °C with an varying oxygen partial pressure in the range of 0.05–0.11 Pa. As the oxygen reactive gas is introduced the Bi metal droplet consumes this gas and develops the nanocone structure. In Fig. 4a) and b) the Bi droplet sits on top of the cones. As the cone grows the metal droplet is reduced, as seen Fig. 4c). The differences between Fig. 3b) and 4c), both exhibiting the pine tree-like nano structures, resides solely in the working gas flow which increased from 40 to 50 sccm, albeit with the same total pressure (0.51 Pa); the pressure was controlled by adjusting the throttle valve between the deposition chamber and the high vacuum turbo pump. In Fig. 4d) the total pressure was increased to 0.90 Pa, via the aforementioned throttle valve adjustment, and it can be perceived that the dendritic structures are suppressed. This microstructural change is ascribed to a decrease in mean free path of the sputtered atoms and hence lower energy when reaching the film growing front, which is rendered insufficient for the dendritic growth of the Bi/Bi_2O_3 layers.

From these optimized conditions of Bi/Bi_2O_3 films, TiO_2 overlayers with thickness between 6 and 30 nm were deposited in order to study the photocatalytic behaviour of these nanostructured templates. The deposition process conditions for the TiO_2 cap layer are presented in Table 2. In can be seen from Fig. 5 that an 18 nm capping layer of TiO_2 just covers the nanocone structures, still preserving in these structures a high surface area.

Fig. 6 shows the X-ray diffraction patterns for Bi/Bi_2O_3 and $Bi/Bi_2O_3/TiO_2$ films. TiO_2 diffraction peaks are not detectable due to the small thickness of the layers, which varies roughly from 6 to 30 nm. From previous experiments with TiO_2 film deposition it was found that a subsequent thermal treatment is required to enhance the film microstructure from amorphous to the development of anatase and rutile crystalline phases [17,22]; this was not performed in these heterostructured films in order to avoid recrystallization of the underlying Bi_2O_3, which impacts on the destruction of the nanocone formation. In all films, Bi (rhombohedral; ICDD card no. 01–085–1331) and β-Bi_2O_3 (tetragonal; ICDD card no. 01–078–1793) phases are detected. Bi metallic phase appears due to the underlying seed layer. According to the literature, β-Bi_2O_3 is a high temperature metastable phase [23,24] and in the present films has a preferential growth of (201) crystallographic planes parallel to the surface, for $2\theta = 27.95°$. The crystallite size is of the order of 50 ± 9 nm for all films and was derived from Rietveld refinement of the diffraction patterns for the preferred orientation of each phase, corresponding to the diffraction planes: Bi (012) at 27.27°; β-Bi_2O_3 (201) at 27.95°. An unassigned peak is marked with (*) for the Bi/Bi_2O_3 film at a diffraction angle of 30.30°, which cannot be indexed to the known Bi and Bi_2O_3 phases. Several authors have reported on the difficulty in indexing XRD patterns involving Bi_2O_3 phases, since for

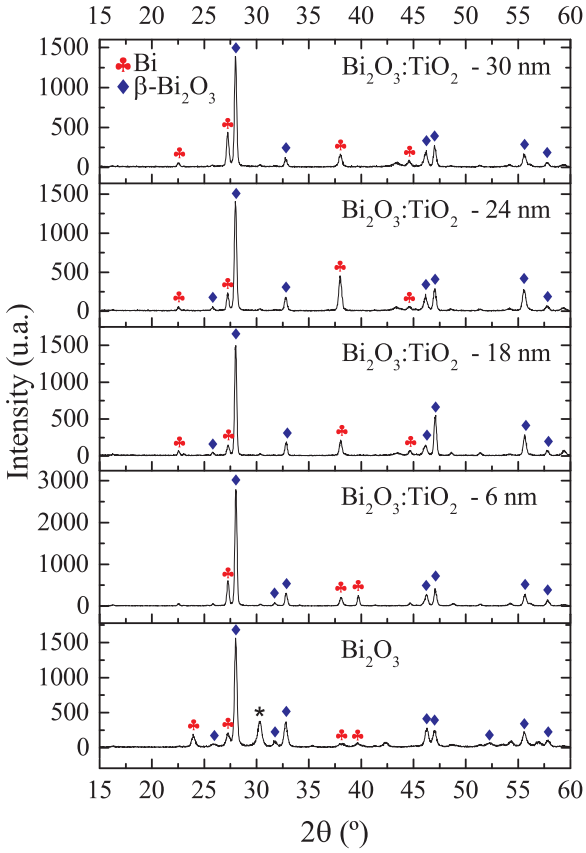

Fig. 6. XRD diffraction patterns taken for Bi/Bi_2O_3 films with varying thickness of TiO_2 layers. A pattern is also represented for a Bi/Bi_2O_3 film.

lower diffraction angles there is a strong chance of superposition of diffraction lines from α-, β- and δ- Bi_2O_3 phases [11,25,26]. In order overcome this limitation, Popa *et al.* studied highly-oriented δ-Bi_2O_3 films stable at RT, deposited by reactive magnetron sputtering, by combining standard XRD with pole figure analysis [25]. From this, the authors unambiguously confirmed the presence of the δ-Bi_2O_3, albeit for a narrow window of deposition process parameters. It should be noted that the latter phase has a fluorite type cubic structure with a high disorder of oxygen vacancies, being more prone to grow in oxygen deficient reactive sputtering [24,25], which is not the present case. Other authors have studied Bi and Bi_2O_3 phases in their materials by Raman spectroscopy where characteristic phonon vibrations can be readily distinguished [26,27]. In the present work, due to the contamination of the samples during the photocatalytic assays in the UV-A reactor, these were rendered unusable for further structural characterization.

Table 3
Roughness and projected surface area values for the deposited layers.

Layer	Roughness (nm)		Projected surface area (μm²)
	R_a	R_q	
Bi	45 ± 2	55 ± 2	9.0 ± 0.1
Bi/Bi_2O_3	52 ± 2	65 ± 3	11.7 ± 0.2

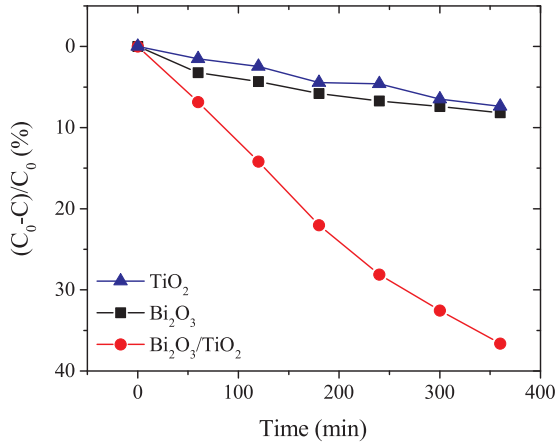

Fig. 8. Degradation kinetics of methylene blue (MB) dye in the presence of TiO_2, Bi_2O_3 and $Bi/Bi_2O_3/TiO_2$ films under UV-A irradiation.

Table 4
Methylene blue dye degradation kinetics.

Sample	k ($\times 10^{-4}$ min^{-1})
Bi/Bi_2O_3	2.2 ± 0.2
$Bi/Bi_2O_3/TiO_2$	13.2 ± 0.3
TiO_2	2.1 ± 0.1

The roughness of the samples was determined from atomic force microscopy analysis, where the mean roughness value, R_a, and root mean square roughness, R_q, was measured for the Bi seed layer and Bi/Bi_2O_3 bilayer template. The AFM micrographs are displayed in Fig. 7 and the roughness results in Table 3. The R_a value is 45 ± 2 nm and 52 nm ± 2 nm for the Bi seed layer and Bi/Bi_2O_3 bilayer template, respectively, however the R_q value, which measures larger displacements form the median surface profile, increases from 55 ± 2 nm to 65 ± 3 nm, respectively. This induced roughness from the dentric growth of the Bi_2O_3 layer is important for enhancing the projected surface area of the film. As with the roughness values, the projected

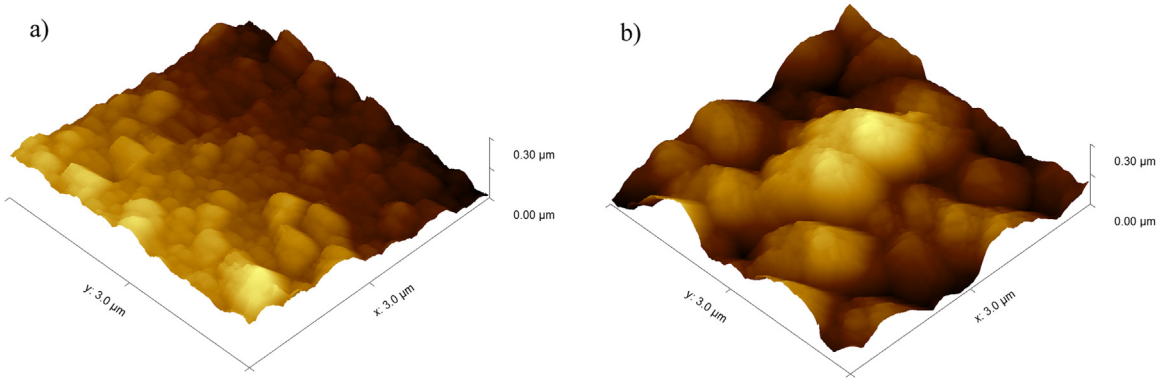

Fig. 7. AFM micrographs of the surface topography of a) Bi and b) Bi/Bi_2O_3 films.

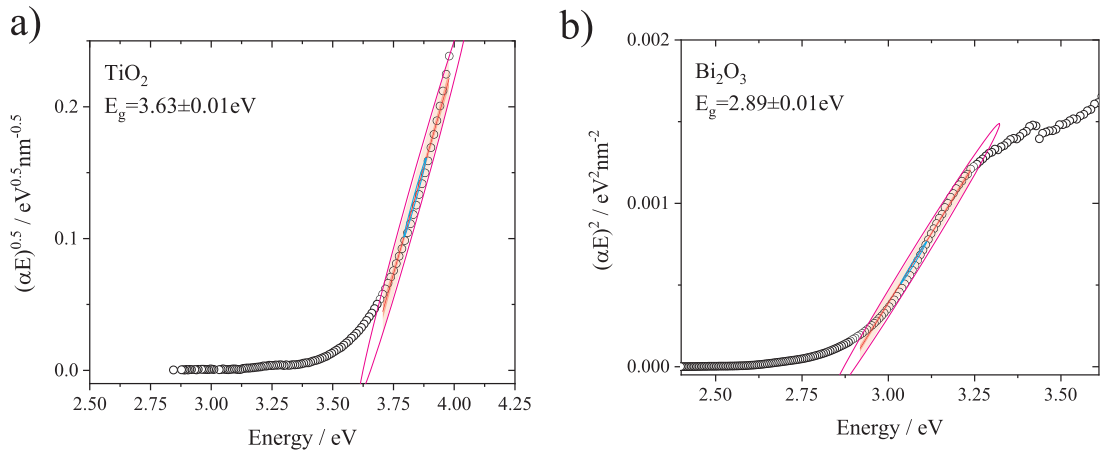

Fig. 9. Tauc plots for the extrapolation of the TiO_2 and Bi_2O_3 band-gaps.

surface area was calculated through statistical algorithms included in the Gwyddion software [28]. The projected surface area can be understood when considering out-of-plane coordinates z_i for $i = 1;2;3;4$, which denote height values in four neighbouring points (pixel centres), and h_x and h_y pixel dimensions along corresponding in-plane axes. If an additional point is placed in the centre of the rectangle, which corresponds to the common corner of the four pixels, four triangles are formed and the projected surface area, A, can be estimated by summing their corresponding areas:

$$A_{12} = \frac{h_x h_y}{4}\sqrt{1+\left(\frac{z_1 - z_2}{h_x}\right)^2 + \left(\frac{z_1 + z_2 - 2\bar{z}}{h_y}\right)^2} \quad (1)$$

$$A = A_{12} + A_{23} + A_{34} + A_{41} \quad (2)$$

The projected surface area is 9.0 ± 0.1 μm^2 and 11.7 ± 0.2 μm^2 for the Bi seed layer and Bi/Bi_2O_3 bilayer template, respectively. Hence, through the dendritic growth of the Bi_2O_3 nanocones the projected surface area is enhanced by ~30%, as expected.

In Fig. 8 the evolution of the kinetics of methylene blue dye degradation can be followed in the presence of TiO_2, Bi_2O_3 and Bi/Bi_2O_3/TiO_2 films under UV-A irradiation (centred at 365 nm). C_0 and C are the initial concentration and concentration at a specific time (t) of the MB dye, which follow a first order kinetics with time: $(C_0-C) = C_0 e^{-kt}$, where k is the first order rate constant. The values of k are given in Table 4 for the deposited films. It can be seen that the Bi/Bi_2O_3/TiO_2 heterostructured film degrades almost 40% of the initial concentration of the dye after 6 h of UV-A illumination, whereas both TiO_2 and Bi_2O_3 individual films do not degrade more than 10% of the initial concentration of the dye under similar conditions. Indeed, for the Bi/Bi_2O_3/TiO_2 heterostructured film, k increases by a factor of 6 when compared to the individual layered films (Table 4). It should be noted that an 18 nm thick TiO_2 film has similar photocatalytic kinetics to a > 1000 nm Bi_2O_3 film. Nevertheless, Bi/Bi_2O_3 films improve photocatalytic efficiency when functionalized with TiO_2, as expected.

From the analysis of Tauc plots in Fig. 9 the optical band-gap (E_g) of individual layers of TiO_2 and Bi_2O_3 on glass substrates, with thickness (d) of 12 nm and 588 nm, were measured to be 3.62 ± 0.01 eV and 2.88 ± 0.01 eV, respectively. For this, optical transmittance (T) and reflectance (R) were recorded and through the calculation of the absorption coefficient, $\alpha = (1/d)\cdot\ln[(100\text{-}R)/T]$ [29] and by subsequently using the relation between the absorption coefficient and photon energy, $\alpha = (A/h\nu)\cdot(h\nu\text{-}E_g)^m$, where A is a parameter independent of the photon energy, hν (h is Planck's constant; ν is photon frequency), and m a value representing the optical transition mode (m = 0.5 for the direct band-gap; m = 2 for the indirect band-gap), E_g was extrapolated from the interception with the photon energy axis, as represented in the Tauc plots of Fig. 9. In the latter linear fitting routine, confidence and prediction bands (> 95%) are shown by the pink lines. The indirect E_g value for TiO_2 is much higher (3.62 eV) when compared to the bulk value reported in the literature (3.20 eV) [30]. The reason for this can be attributed to the fact that the TiO_2 thin film layer is only 12 nm thick and amorphous. For thicker and more crystalline TiO_2 films the E_g value would approximate the bulk value. Conversely, the E_g value for the Bi_2O_3 layer is similar to what has been reported in the literature Bi_2O_3 films with direct band-gap, between 2.8 and 2.9 eV [21,27,31]. Due to the coupling effect of the two semiconductors that reduce the optical band-gap, there is an enhancement in the photocatalytic efficiency, as observed in Fig. 8 and Table 4.

4. Conclusions

In this work, under optimized deposition process conditions, Bi_2O_3 films with a dendritic growth of nanocone-like structures were deposited by magnetron sputtering, through a vapour-liquid-solid mechanism from a starting Bi seed layer. AFM measurements provided the assessment of the roughness and projected surface area of the Bi seed layer and Bi/Bi_2O_3 template bilayer, which enhanced substantially, ~15% and ~30%, respectively, for the latter case. From measurements of the degradation kinetics of MB dye under UV-A illumination it was resolved that the photocatalytic efficiency increases by a factor of 6 when the Bi_2O_3 nanocones template are functionalized with a capping TiO_2 thin film. Hence, it can be concluded that the heterogeneous junction of Bi_2O_3/TiO_2 semiconductors registers enhanced photocatalytic efficiency. Furthermore, the formation of nanocones is crucial for high specific surface area with potential applications for water and air decontamination.

Acknowledgements

The authors acknowledge the funding from the Portuguese institution *Fundação para a Ciência e Tecnologia*, through the Strategic project reference UID/FIS/04650/2013, Ph.D grant SFRH/BD/111720/2015 for Filipe C. Correia and Ph.D grant SFRH/BD/112868/2015 Juliana Marques.

References

[1] S. Malato, P. Fernández-Ibáñez, M.I. Maldonado, J. Blanco, W. Gernjak, Decontamination and disinfection of water by solar photocatalysis: recent overview and trends, Catal. Today 147 (2009) 1–59, https://doi.org/10.1016/J.CATTOD.2009.06.018.

[2] K. Nakata, A. Fujishima, TiO2 photocatalysis: design and applications, J. Photochem. Photobiol. C. Photochem. Rev. 13 (2012) 169–189, https://doi.org/10.1016/j.jphotochemrev.2012.06.001.

[3] A. Fujishima, X. Zhang, Titanium dioxide photocatalysis: present situation and future approaches, Comptes Rendus Chim. 9 (2006) 750–760, https://doi.org/10.

1016/j.crci.2005.02.055.
[4] A. Mills, S.K. Lee, A web-based overview of semiconductor photochemistry-based current commercial applications, J. Photochem. Photobiol. A Chem. 152 (2002) 233–247, https://doi.org/10.1016/S1010-6030(02)00243-5.
[5] A.L. Linsebigler, A.L. Linsebigler, J.T. Yates Jr, G. Lu, G. Lu, J.T. Yates, Photocatalysis on TiO2 Surfaces: principles, Mechanisms, and Selected Results, Chem. Rev. 95 (1995) 735–758, https://doi.org/10.1021/cr00035a013.
[6] L. Leontie, M. Caraman, M. Alexe, C. Harnagea, Structural and optical characteristics of bismuth oxide thin films, Surf. Sci. 507– 510 (2002) 480–485, https://doi.org/10.1016/S0039-6028(02)01289-X.
[7] B. Sirota, J. Reyes-Cuellar, P. Kohli, L. Wang, M.E. McCarroll, S.M. Aouadi, Bismuth oxide photocatalytic nanostructures produced by magnetron sputtering deposition, Thin Solid Films. 520 (2012) 6118–6123, https://doi.org/10.1016/j.tsf.2012.06.001.
[8] J. Hou, C. Yang, Z. Wang, W. Zhou, S. Jiao, H. Zhu, In situ synthesis of α-β phase heterojunction on Bi2O3nanowires with exceptional visible-light photocatalytic performance, Appl. Catal. B Environ. 142–143 (2013) 504–511, https://doi.org/10.1016/j.apcatb.2013.05.050.
[9] L. Zhou, W. Wang, H. Xu, S. Sun, M. Shang, Bi_2O_3 hierarchical nanostructures: controllable synthesis, growth mechanism, and their application in photocatalysis, Chem. - A Eur. J. 15 (2009) 1776–1782, https://doi.org/10.1002/chem.200801234.
[10] J.C. Medina, M. Bizarro, C.L. Gomez, O. Depablos-Rivera, R. Mirabal-Rojas, B.M. Monroy, et al., Sputtered bismuth oxide thin films as a potential photocatalytic material, Catal. Today 266 (2016) 144–152, https://doi.org/10.1016/j.cattod.2015.10.025.
[11] K. Brezesinski, R. Ostermann, P. Hartmann, J. Perlich, T. Brezesinski, Exceptional photocatalytic activity of ordered mesoporous??-Bi 2O3 thin films and electrospun nanofiber mats, Chem. Mater. 22 (2010) 3079–3085, https://doi.org/10.1021/cm903780m.
[12] J. Zhang, I. Boyd, B. OSULLIVAN, P. HURLEY, P. KELLY, J. Senateur, Nanocrystalline TiO2 films studied by optical, XRD and FTIR spectroscopy, J. Non Cryst. Solids 303 (2002) 134–138, https://doi.org/10.1016/S0022-3093(02)00973-0.
[13] H. Cheng, B. Huang, J. Lu, Z. Wang, B. Xu, X. Qin, et al., Synergistic effect of crystal and electronic structures on the visible-light-driven photocatalytic performances of Bi2O3 polymorphs, Phys. Chem. Chem. Phys. 12 (2010) 15468, https://doi.org/10.1039/c0cp01189d.
[14] L. Wang, J. Zhang, C. Li, H. Zhu, W. Wang, T. Wang, Synthesis, characterization and photocatalytic activity of TiO2 Film/Bi2O3 microgrid heterojunction, J. Mater. Sci. Technol. 27 (2011) 59–63, https://doi.org/10.1016/S1005-0302(11)60026-1.
[15] P. Yang, H. Yan, S. Mao, R. Russo, J. Johnson, R. Saykally, et al., Controlled growth of ZnO nanowires and their optical properties, Adv. Funct. Mater. 12 (2002) 323, https://doi.org/10.1002/1616-3028(20020517)12:5<323::AID-ADFM323>3.0.CO;2-G.
[16] C.J. Tavares, S.M. Marques, T. Viseu, V. Teixeira, J.O. Carneiro, E. Alves, et al., Enhancement in the photocatalytic nature of nitrogen-doped PVD-grown titanium dioxide thin films, J. Appl. Phys. 106 (2009) 113535, https://doi.org/10.1063/1.3269702.
[17] C.J. Tavares, J. Vieira, L. Rebouta, G. Hungerford, P. Coutinho, V. Teixeira, et al., Reactive sputtering deposition of photocatalytic TiO2 thin films on glass substrates, Mater. Sci. Eng. B. 138 (2007) 139–143, https://doi.org/10.1016/j.mseb.2005.11.043.
[18] R.S. Wagner, W.C. Ellis, Vapor-liquid-solid mechanism of single crystal growth, Appl. Phys. Lett. 4 (1964) 10–12, https://doi.org/10.1063/1.1753975.
[19] E.A. Stach, P.J. Pauzauskie, T. Kuykendall, J. Goldberger, R. He, P. Yang, Watching GaN nanowires grow, Nano Lett. 3 (2003) 867–869, https://doi.org/10.1021/nl034222h.
[20] L. Kumari, J. Lin, Y. Ma, One-dimensional Bi2O3 nanohooks: synthesis, characterization and optical properties, J. Phys. Condens. Matter 406204 (2007) 1–11, https://doi.org/10.1088/0953-8984/19/40/406204.
[21] L. Tien, Y. Liou, Synthesis of Bi2O3 nanocones over large areas by magnetron sputtering, Surf. Coat. Technol. 265 (2015) 1–6, https://doi.org/10.1016/j.surfcoat.2015.01.072.
[22] D. Rodrigues, P. Teixeira, C.J. Tavares, J. Azeredo, Food contact surfaces coated with nitrogen-doped titanium dioxide: effect on Listeria monocytogenes survival under different light sources, Appl. Surf. Sci. 270 (2013) 1–5, https://doi.org/10.1016/j.apsusc.2012.11.119.
[23] M. Drache, P. Roussel, J.P. Wignacourt, Structures and oxide mobility in Bi-Ln-O materials: heritage of Bi2O3, Chem. Rev. 107 (2007) 80–96, https://doi.org/10.1021/cr050977s.
[24] H.T. Fan, S.S. Pan, X.M. Teng, C. Ye, G.H. Li, Structure and thermal stability of δ-Bi_2O_3 thin films deposited by reactive sputtering, J. Phys. D. Appl. Phys. 39 (2006) 1939–1943, https://doi.org/10.1088/0022-3727/39/9/032.
[25] P. Lunca Popa, S. Sønderby, S. Kerdsongpanya, J. Lu, N. Bonanos, P. Eklund, Highly oriented δ-Bi_2O_3 thin films stable at room temperature synthesized by reactive magnetron sputtering, J. Appl. Phys. 113 (2013) 046101, https://doi.org/10.1063/1.4789597.
[26] C.L. Gomez, O. Depablos-rivera, P. Silva-bermudez, S. Muhl, A. Zeinert, M. Lejeune, et al., Opto-electronic properties of bismuth oxide films presenting different crystallographic phases, Thin Solid Films. 578 (2015) 103–112, https://doi.org/10.1016/j.tsf.2015.02.020.
[27] C.-H. Ho, C.-H. Chan, Y.-S. Huang, L.-C. Tien, L.-C. Chao, The study of optical band edge property of bismuth oxide nanowires α-Bi_2O_3, Opt. Express 21 (2013) 11965, https://doi.org/10.1364/OE.21.011965.
[28] D. Nečas, P. Klapetek, Gwyddion: an open-source software for SPM data analysis, Cent. Eur. J. Phys. (2012), https://doi.org/10.2478/s11534-011-0096-2.
[29] J. Rodríguez, M. Gómez, J. Ederth, G.A. Niklasson, C.G. Granqvist, Thickness dependence of the optical properties of sputter deposited Ti oxide films, Thin Solid Films 365 (2000) 119–125, https://doi.org/10.1016/S0040-6090(99)01109-8.
[30] A. Fujishima, X. Zhang, D.A. Tryk, Surface Science Reports TiO 2 photocatalysis and related surface phenomena, 63, 2008, pp. 515–582. doi: 10.1016/j.surfrep.2008.10.001.
[31] J. Morasch, S. Li, J. Brötz, W. Jaegermann, A. Klein, Reactively magnetron sputtered Bi2O3 thin films: analysis of structure, optoelectronic, interface, and photovoltaic properties, Phys. Status Solidi Appl. Mater. Sci. 211 (2014) 93–100, https://doi.org/10.1002/pssa.201330216.